


## Article

# Water-Assisted Cold Sintering of Alumina Ceramics in SPS Conditions

Anastasia A. Kholodkova <sup>1,\*</sup> , Maxim V. Korniyushin <sup>1</sup>, Mikhail A. Pakhomov <sup>1</sup>, Andrey V. Smirnov <sup>2</sup> and Yurii D. Ivakin <sup>3,4</sup>

<sup>1</sup> Statistics Department, Department of Scientific Research Coordination, State University of Management, 109545 Moscow, Russia

<sup>2</sup> Laboratory of Ceramic Materials and Technologies, MIREA—Russian Technological University, 119454 Moscow, Russia

<sup>3</sup> Mobile Solutions Engineering Center, MIREA—Russian Technological University, 119454 Moscow, Russia

<sup>4</sup> Chemistry Department, M.V. Lomonosov Moscow State University, 119991 Moscow, Russia

\* Correspondence: anastasia.kholodkova@gmail.com

**Abstract:** A developing energy-saving approach of cold sintering in a pure aqueous medium was applied to the preparation of  $\alpha$ -Al<sub>2</sub>O<sub>3</sub> ceramics and performed on spark plasma sintering equipment. The initial  $\gamma$ -Al(OH)<sub>3</sub> and  $\gamma$ -AlOOH powders and the cold-sintered ceramics were studied by X-ray diffraction analysis, infrared spectroscopy, thermal analysis, and scanning electron microscopy to reveal the chemical and structural transformations they experienced during the cold sintering. At 450 °C and 70 MPa, initially  $\gamma$ -AlOOH transformed into a fragile  $\alpha$ -Al<sub>2</sub>O<sub>3</sub> material. Porous  $\alpha$ -Al<sub>2</sub>O<sub>3</sub> ceramics with about 60% porosity were obtained after cold sintering of  $\gamma$ -Al(OH)<sub>3</sub> in the same conditions combined with subsequent annealing at 1250 °C for 3 h. The role of water molecules in the studied processes was considered as the enhancement of structural mobility in the cold-sintered material due to its reversible hydroxylation similar to earlier investigated supercritical water actions on the precursors during  $\alpha$ -Al<sub>2</sub>O<sub>3</sub> formation. Further improvement of the cold sintering setup and regimens would open prospects in  $\alpha$ -Al<sub>2</sub>O<sub>3</sub> ceramics manufacturing by an ecologically benign route.

**Keywords:** cold sintering; alumina ceramics; spark plasma sintering; vapor; porous ceramics; post-annealing; microstructure



**Citation:** Kholodkova, A.A.; Korniyushin, M.V.; Pakhomov, M.A.; Smirnov, A.V.; Ivakin, Y.D. Water-Assisted Cold Sintering of Alumina Ceramics in SPS Conditions. *Ceramics* **2023**, *6*, 1113–1128. <https://doi.org/10.3390/ceramics6020066>

Academic Editors: Margarita A. Goldberg and Elisa Torresani

Received: 9 April 2023  
Revised: 6 May 2023  
Accepted: 15 May 2023  
Published: 17 May 2023



**Copyright:** © 2023 by the authors. Licensee MDPI, Basel, Switzerland. This article is an open access article distributed under the terms and conditions of the Creative Commons Attribution (CC BY) license (<https://creativecommons.org/licenses/by/4.0/>).

## 1. Introduction

Dense as well as porous alumina ceramics are well-known technical materials with quite a few applications in the industry of corrosion- and wear-resistant components, catalysis, filtration, thermal insulation, sound absorption, tissue engineering, etc. These materials are highly appreciated due to their thermal and chemical stability, excellent mechanical strength, and low thermal expansion. Green bodies for dense ceramics are usually shaped by dry and isostatic pressing. To create the desired porosity in alumina ceramics, different approaches have been employed [1] such as partial sintering [2,3], sacrificial templating [4–6], replica technique [7,8], direct foaming [9,10] combined with different types of shaping techniques (pressing, casting, additive manufacturing, etc.).

A significant technological difficulty of alumina ceramics is the rather high energy consumption in the stage of its sintering. Commonly, in conventional ceramics sintering, the temperatures of 50–75% of the material's melting point are applied. In the case of alumina, it exceeds 1400 °C [11], while the leucosapphire by Verneuil, Bagdasarov, Stepanov, Bridgen, or Kyropoulos methods is produced at temperatures above the alumina melting point (2072 °C). In recent decades, a few innovative sintering approaches have been introduced combining high heating rates and pressure application, for example, hot pressing [12], hot isostatic pressing [13], microwave sintering [14], field-assisted sintering technology (FAST) [15], and spark plasma sintering (SPS) [16]. The development of these techniques

aimed to lower the energy consumption and the environmental impact of the ceramics production. For example, the fabrication of dense [17,18] or porous [19] alumina ceramics by SPS still requires high temperatures of 1400–1500 °C with an exception to those prepared from nanopowders [20]. However, due to the pulse current, rapid well-controllable heating, and simultaneous mechanical pressing, this technique allows significant shortening of the sintering duration to tens of minutes, thus reducing the energy budget. In terms of lowering the sintering temperature, the cold sintering process (CSP) seems the most promising among the emerging sintering approaches [21,22]. Commonly, CSP includes uniaxial pressing of the oxide powders at 50–500 MPa in the presence of a liquid (acid or alkaline aqueous solutions) on heating below 350 °C [11]. Mainly, the studies of CSP are focused on the preparation of zinc oxide [23–30] as well as ferro- and piezoelectric ceramics (BaTiO<sub>3</sub> [31–34], (K,Na)NbO<sub>3</sub> [35–38], and Pb(Zr,Ti)O<sub>3</sub> [39–41]). Alumina ceramics remain an attractive but a “difficult” object for this processing technique. For the moment, only several studies described the manufacturing of Al<sub>2</sub>O<sub>3</sub>–NaCl [42,43] and Al<sub>2</sub>O<sub>3</sub>–hydroxyapatite [44] composites by cold sintering. Hérisson de Beauvoir et al. [45] performed the efforts of Al<sub>2</sub>O<sub>3</sub> ceramics fabrication with the use of CSP. In this work, starting Al(OH)<sub>3</sub>·xH<sub>2</sub>O was treated under CSP conditions at 150–400 °C and 500 MPa for 30–180 min to obtain dense semi-transparent samples containing amorphous alumina and boehmite γ-AlOOH. After heating at 500 °C, the samples transformed into γ-Al<sub>2</sub>O<sub>3</sub> completely. Kang et al. [46] successfully prepared ~98% dense α-Al<sub>2</sub>O<sub>3</sub> ceramics by CSP of a mixture of α- and γ-Al<sub>2</sub>O<sub>3</sub> powders at 300 °C and 300 MPa for 60 min, in a glacial acetic acid medium with the second sintering in air above 1250 °C. These results demonstrated the capability of the CPS method to fabricate comparatively dense alumina and related ceramic materials. Additionally, Suleiman et al. [43] demonstrated the use of NaCl as a pore-forming agent as well as a sintering aid at the stage of post-annealing in air at 1200–1500 °C.

There are several works reporting ceramics preparation by a hybrid CSP/SPS approach. First of all, this approach allowed for sintering with densification above 90% of so called “thermodynamically fragile materials” such as MnSO<sub>4</sub>, Na<sub>2</sub>Cu(CO<sub>3</sub>)<sub>2</sub>, K<sub>2</sub>Cu(CO<sub>3</sub>)<sub>2</sub>, and NH<sub>4</sub>FeP<sub>2</sub>O<sub>7</sub> [47]. The sintering featured hydrated starting powders, which performed with higher thermal stability in SPS than in air conditions, and were successfully consolidated below 400 °C. The FAST/SPS technique considerably contributed to the development of the ZnO cold sintering processing as it elucidated the role of the trapped water in the material densification on high heating rates [24,25,48]. Later, ZnO ceramics with density up to 99% of the theoretical were derived by the CSP/SPS or FAST/SPS/CSP techniques at only 250–300 °C and 50–150 MPa for only 5 min exposure with the addition of water [49,50], acetic acid [51], or zinc acetate and water [52]. Despite the obvious potential, the number of ceramic compositions produced by the mentioned approach remains quite modest and applies only to dense ceramics. The current work is aimed at expanding the range of these compositions by the preparation of α-alumina ceramics using CSP-SPS conditions. Compared to most of the works mentioned above and devoted to CSP of alumina ceramics, here, we avoid the use of any auxiliary substances except for pure water. Additionally, the initial materials are chosen in hydroxylated forms (hydrargillite γ-Al(OH)<sub>3</sub> and boehmite γ-AlOOH). These ideas originated from the earlier results on the synthesis of α-Al<sub>2</sub>O<sub>3</sub> from the same precursors in supercritical water [53]. According to the mentioned results, the interaction of the precursors with supercritical water led to the appearance of a solid-state mobility in their structures which favored α-Al<sub>2</sub>O<sub>3</sub> formation at only 400 °C. Supposedly, the combined effect of mechanical pressure and aqueous medium in CSP-SPS would contribute to α-alumina ceramics formation. Furthermore, the results of this work would expand understanding of the role of water in the CSP of ceramic materials including Al<sub>2</sub>O<sub>3</sub>.

## 2. Materials and Methods

Commercial hydrargillite γ-Al(OH)<sub>3</sub> powder (Pikalevo Alumina Refinery LLC, Pikalevo, Russia) with a purity of >99.6 wt.% and boehmite powder γ-AlOOH were used as starting

materials for ceramics processing.  $\gamma$ -AlOOH was synthesized from  $\gamma$ -Al(OH)<sub>3</sub> by its treatment in supercritical water as follows. The initial  $\gamma$ -Al(OH)<sub>3</sub> powder was placed into a stainless steel container inside a laboratory stainless steel autoclave. The required amount of distilled water was poured into the autoclave outside the container with  $\gamma$ -Al(OH)<sub>3</sub>. Further, the autoclave was sealed and heated up to 400 °C with a rate of 200 °C h<sup>-1</sup>. The pressure of supercritical water during the synthesis reached 26.0 MPa. After 5 h of exposure, the autoclave was drastically cooled down to room temperature, the obtained product was removed from it, and dried in air at 70 °C for 10 h.

To provide alumina nucleation [54] during the cold sintering,  $\alpha$ -Al<sub>2</sub>O<sub>3</sub> powder (Treibacher Industrie AG, Althofen, Austria) in an amount of 5 wt.% was added to  $\gamma$ -Al(OH)<sub>3</sub> as well as to  $\gamma$ -AlOOH by joint sieving through a sieve with a 300 µm cell. Densification of the prepared mixtures was conducted with use of the SPS machine H-HP D 25 (FCT Systeme, GmbH, Rauenstein, Germany) with a conventional graphite mold of 20 mm in diameter. During the SPS experiments, the mold containing the initial powder mixture and 5 wt.% of distilled water was exposed to a pressure of 70 MPa and heated up to 450 °C with a rate of 300 °C min<sup>-1</sup>. After reaching 450 °C, the mold was kept at this temperature for 20 min and then cooled to room temperature without an applied pressure. The surfaces of the prepared ceramic samples were mechanically cleared from graphlex residues. The samples prepared from the  $\gamma$ -Al(OH)<sub>3</sub> powder were further annealed at 1250 °C for 3 h in air with the heating rate of 250 °C h<sup>-1</sup> following the previously reported data [46]. The labeling of the obtained ceramic samples is collected in Table 1.

**Table 1.** Samples prepared by CSP-SPS and the following annealing in air.

Initial Powder	Samples after CSP-SPS	Samples after Annealing in Air
$\gamma$ -Al(OH) <sub>3</sub> (HA-P)	HA-CS	HA-CS-A
$\gamma$ -AlOOH (BO-P)	BO-CS	-

The phase contents of the starting powders and the prepared ceramics after their thorough grinding were studied by the means of the Rigaku D/Max-2500 (Rigaku Corporation, Tokyo, Japan) X-ray diffractometer in a range of 10° < 2 $\theta$  < 70° with a step of 0.02°. The phases were identified by comparing the obtained patterns with the data from the PDF-2 database [55]. The JSM-6380 LA (JEOL Ltd., Tokyo, Japan) scanning electron microscope was used to observe the morphology of the powders and the fractured surfaces of the ceramics. Particle and grain sizes were estimated by linear segment measurements in the SEM images using ImageJ software [56]. Thermal analysis was performed by a combined TG-DSC analyzer STA 449C Jupiter with a mass-spectrometer QMS 403 C Aeolos (Netzsch GmbH, Selb, Germany). The ceramic sample was heated with a rate of 10° min<sup>-1</sup> in the range of 40–1000 or 40–1200 °C in a flow of air. Infrared spectra were studied by diffuse reflectance infrared Fourier transform spectroscopy (DRIFTS) in a range of 400–4000 cm<sup>-1</sup> with the use of the IR Fourier spectrometer EQUINOX 55/S (Bruker Co., Billerica, MA, USA). Apparent density of the ceramic samples was determined by the Archimedes method using kerosene as a saturating liquid.

### 3. Results

The initial  $\gamma$ -Al(OH)<sub>3</sub> powder consisted of mostly prismatic particles with the mean size of 3.46 µm. The starting  $\gamma$ -AlOOH powder contained finer particles of about 0.65 µm in size on average which possessed plate-like shapes (Figure 1).

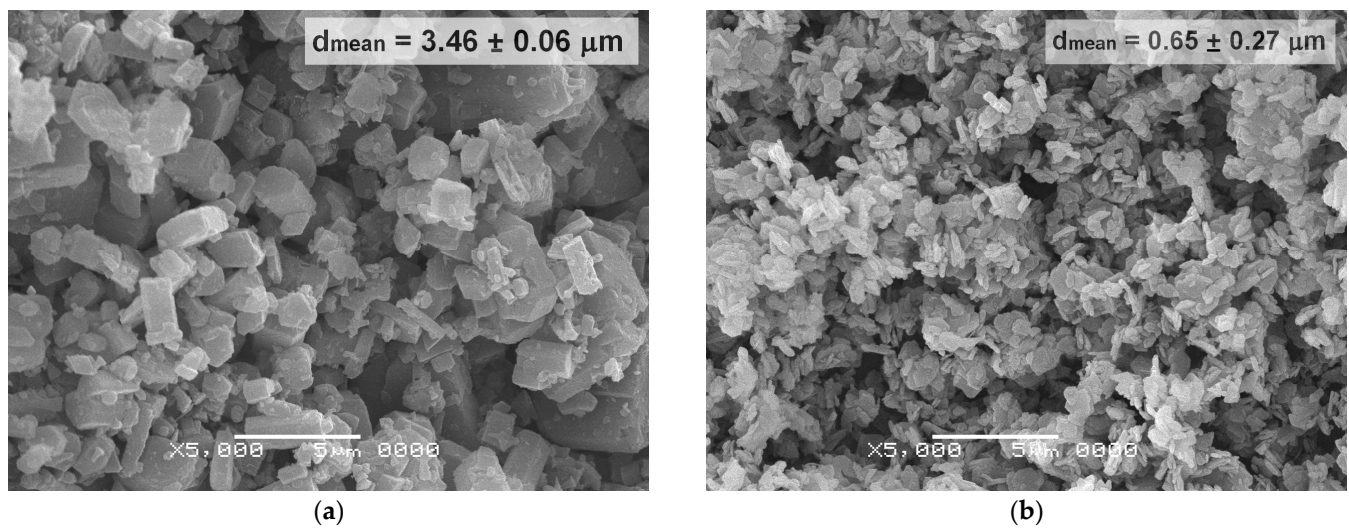


**Figure 1.** Initial powder morphology: (a) Hydrargillite  $\gamma\text{-Al(OH)}_3$ ; (b) Boehmite  $\gamma\text{-AlOOH}$ .

Figure 2 shows the results of the XDR analysis of ceramic samples obtained from hydrargillite powder by the CSP (sample HA-CS) as well as by further annealing in air at 1250 °C (sample HA-CS-A). The cold sintering led to the phase transformation of  $\gamma\text{-Al(OH)}_3$  into boehmite (PDF2 #00-074-1895) and  $\gamma\text{-Al}_2\text{O}_3$  (PDF2 #00-029-0063). The presence of  $\alpha\text{-Al}_2\text{O}_3$  in this sample was attributed to the alumina powder initially added to hydrargillite in the amount of 5 wt.%. To promote transformation of the bulk into  $\alpha$ -alumina, the sample was treated at high temperature. After the annealing of these cold-sintered ceramics,  $\alpha\text{-Al}_2\text{O}_3$  (PDF2 #00-010-0173) became the main phase in the sample along with traces of  $\beta\text{-Al}_2\text{O}_3$  (PDF2 #00-010-0414). The least is known as layer-structured oxide with a composition  $x\text{Na}_2\text{O} \cdot 11\text{Al}_2\text{O}_3$  where  $x$  is from the range of 1.0–1.6 [57]. Its formation could be explained by the probable presence of the  $\text{Na}_2\text{O}$  admixture in the  $\gamma\text{-Al(OH)}_3$  powder initially used in the experiment.

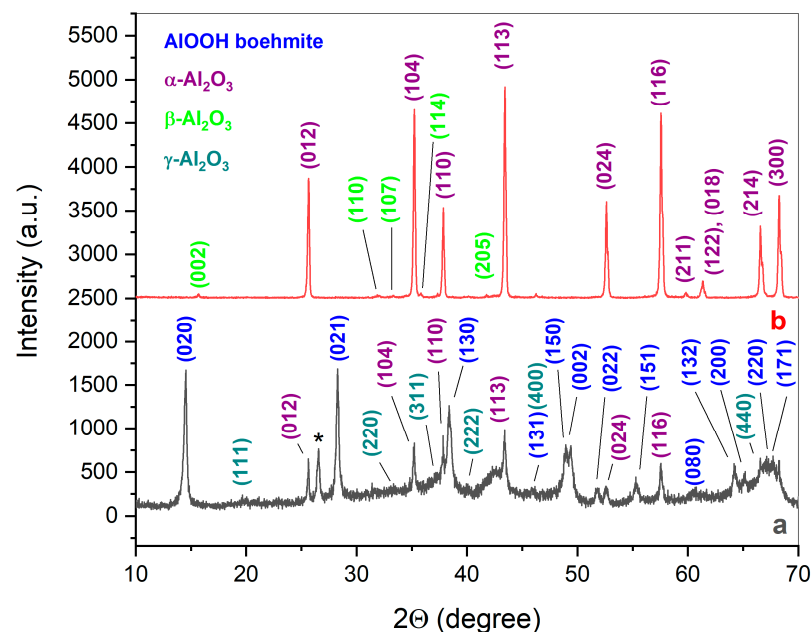


**Figure 2.** XRD patterns of ceramic samples prepared from the mixture of 95 wt.%  $\gamma\text{-Al(OH)}_3$  and 5 wt.%  $\alpha\text{-Al}_2\text{O}_3$ : (a) As-sintered via CSP-SPS; (b) Annealed at 1250 °C for 3 h in air after CSP-SPS. Miller indices are colored as the phases mentioned in the left upper angle of the figure, correspondingly. Asterisk (\*) indicates carbon contamination (PDF2 #00-026-1076).



After the treatment of hydrargillite powder in supercritical water at 400 °C and 26 MPa for 5 h, boehmite (PDF2 #00-074-1895) with a minor phase of  $\alpha$ -Al<sub>2</sub>O<sub>3</sub> (PDF2 #00-010-0173) was obtained (Figure 3a). Boehmite formation in these conditions was expected from the previously reported data [58]. Cold sintering of this powder mixed with an additional 5 wt.% of  $\alpha$ -alumina led to its full transformation into  $\alpha$ -Al<sub>2</sub>O<sub>3</sub> as it was performed by XRD (Figure 3b).

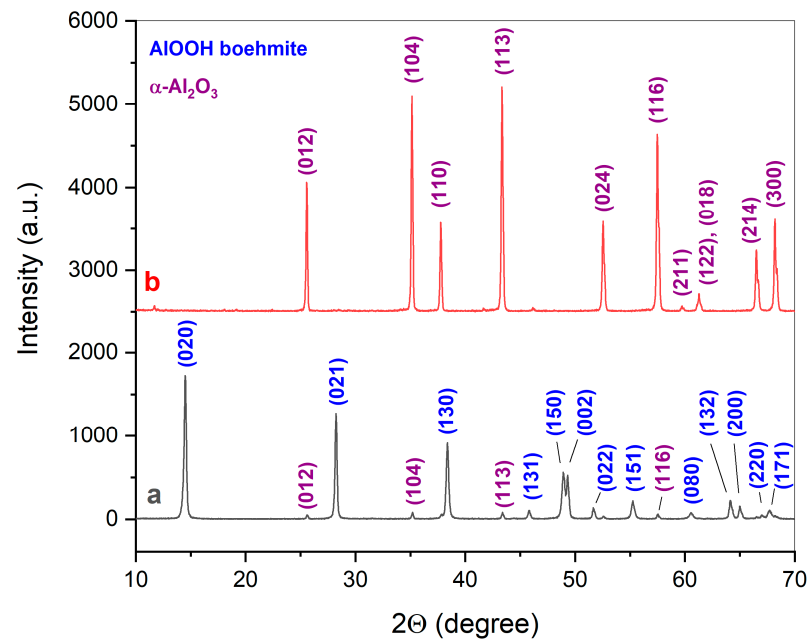


**Figure 3.** XRD patterns of the samples: (a) The synthesized  $\gamma$ -AlOOH; (b) Ceramics as-sintered via CSP-SPS from the mixture of 95 wt.%  $\gamma$ -AlOOH and 5 wt.%  $\alpha$ -Al<sub>2</sub>O<sub>3</sub> powders. Miller indices are colored as the phases mentioned in the left upper angle of the figure.

The thermal analysis of the initial hydrargillite powder HA-P (Figure 4a) showed its rather typical behavior in the case of coarse particles, with a shift of the effects on the DSC curve towards higher temperatures compared to earlier data [59]. Endo-effects observed at 245.2 and 324.6 °C corresponded to the gradual formation of boehmite from  $\gamma$ -Al(OH)<sub>3</sub> as well as the formation of the transient Al<sub>2</sub>O<sub>3</sub> phase from this newly formed  $\gamma$ -AlOOH. The mentioned processes were accompanied by the most significant weight loss at the TG curve (over 25 wt.%). Next, the endothermic peak at 522.8 °C displayed termination of the transition from boehmite to  $\gamma$ -Al<sub>2</sub>O<sub>3</sub> [60,61] with the corresponding losses of about 6 wt.%. The chosen heating rate of 10 °C min<sup>−1</sup> appeared fast enough to hide the effect of further  $\gamma$ - to  $\delta$ -alumina transition at the DSC curve [60]. However, there was a visible exothermic peak at 1080.2 °C, which could accompany either  $\delta$ - to  $\theta$ -Al<sub>2</sub>O<sub>3</sub> or  $\theta$ - to  $\alpha$ -Al<sub>2</sub>O<sub>3</sub> transformation. Following the literature, this temperature was fairly low for  $\alpha$ -alumina formation [62]; however, the  $\theta$ - to  $\alpha$ -Al<sub>2</sub>O<sub>3</sub> transformation was also reported to occur from 1050 °C [60]. Additionally, the lowering of the transition temperature could be associated with the initial presence of  $\alpha$ -Al<sub>2</sub>O<sub>3</sub> in the studied sample.

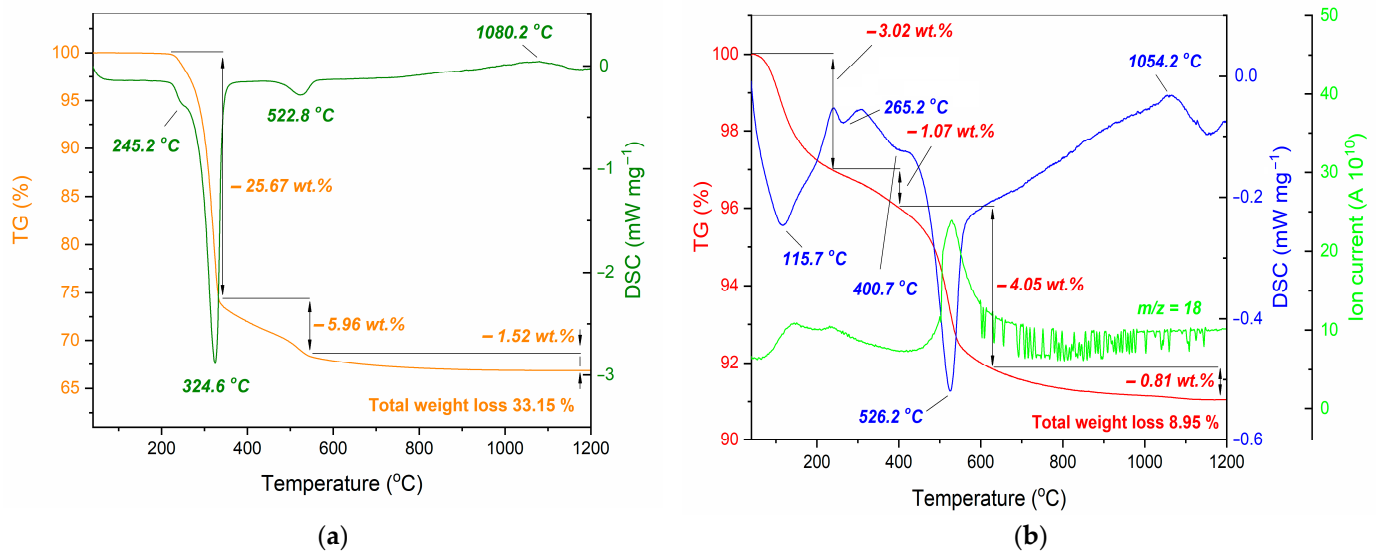


**Figure 4.** Thermal analysis for the samples: (a) The initial  $\gamma$ -Al(OH)<sub>3</sub> powder; (b) Sample as-sintered by CSP-SPS from the mixture of 95 wt.%  $\gamma$ -Al(OH)<sub>3</sub> and 5 wt.%  $\alpha$ -Al<sub>2</sub>O<sub>3</sub> powders ( $m/z$ —ion mass to charge ratio corresponding to H<sub>2</sub>O<sup>+</sup>).

The thermal behavior of the ceramic sample obtained from the mixture of 95 wt.%  $\gamma$ -Al(OH)<sub>3</sub> and 5 wt.%  $\alpha$ -Al<sub>2</sub>O<sub>3</sub> (HA-CS) is shown in Figure 4b. It demonstrated a considerable content of physisorbed water (above 3 wt.%) and chemisorbed water (about 1 wt.%) gradually emitted up to 300 °C. This process was followed by boehmite decomposition to  $\gamma$ -Al<sub>2</sub>O<sub>3</sub> with endo-effects at 400.7 and 526.2 °C. Previously, boehmite was reported to lose hydroxyl groups during its thermal decomposition in two stages [63]. First, weakly bonded OH-groups were eliminated while the boehmite structure was preserved. Then, strongly bonded hydroxyl groups left boehmite during its transformation into alumina. Worth noting that the less defective boehmite possessed a lower amount of weakly bonded hydroxyls and showed a higher transformation temperature. In the mass spectrum, water emission occurred together with the processes of its release mentioned above (Figure 4b).

The temperature of the weight losses and the heat effects recorded for boehmite powder BO-P synthesized in supercritical water (Figure 5a) corresponded well to those observed in ceramics HA-CS and related to the  $\gamma$ -AlOOH transformation into  $\gamma$ -Al<sub>2</sub>O<sub>3</sub> (Figure 4b). Again, boehmite decomposition occurred in two steps with endo-effects at 396.2 and 533.8 °C. A slight shift of the second endo-effect to a higher temperature compared to the sample HA-CS was associated with the less defective structure of  $\gamma$ -AlOOH obtained by the synthesis in supercritical water [63]. The conditions of boehmite powder synthesis in an aqueous medium and its duration favored both hydroxylation and dehydroxylation in its structure which led to the defect elimination. The exothermic peak at 916.2 °C was likely to accompany a transition between Al<sub>2</sub>O<sub>3</sub> modifications. The observed total weight loss of about 17 wt.% corresponded well to the calculated value for boehmite transformation into alumina considering the adsorbed water. The TG and DSC curves of the ceramic sample BO-CS showed the adsorbed water ejections with endo-effects at 99.1 and 248.5 °C. Additionally, an exo-effect at 956.0 °C pointed to the presence of residual Al<sub>2</sub>O<sub>3</sub> transient phases along with the main phase of  $\alpha$ -alumina. The shape of these curves resembled those registered for a commercial  $\alpha$ -alumina powder (Figure A1). However, the release of water at about 250–265 °C inherent for the prepared ceramics (HA-CS and BO-CS) appeared as a footprint of the cold sintering process they experienced.

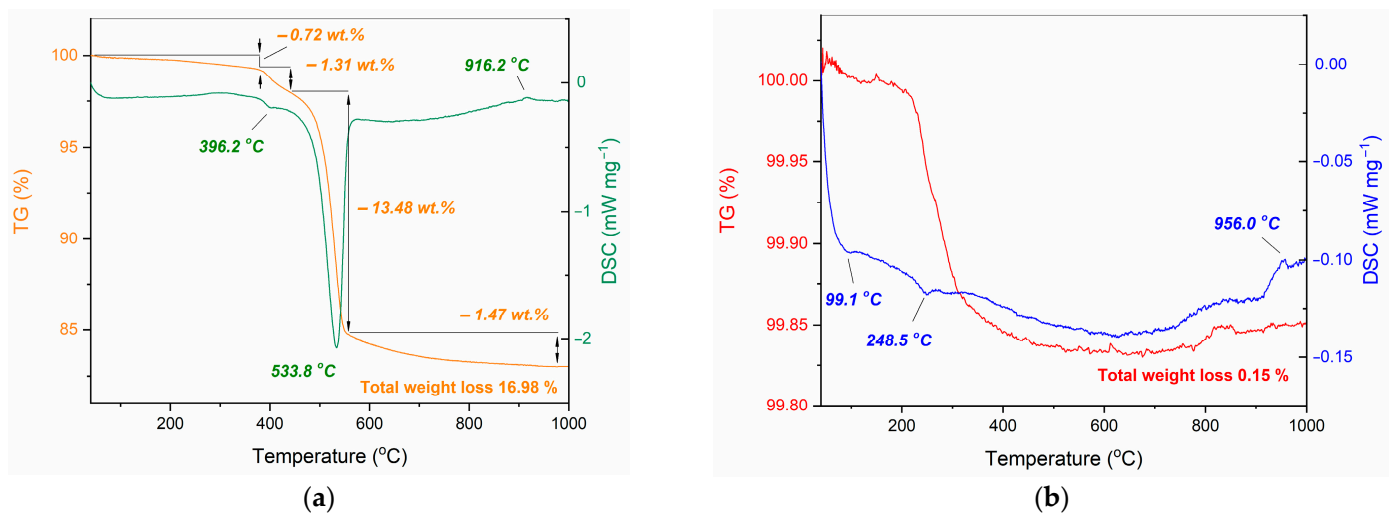


**Figure 5.** Thermal analysis for the samples: (a) The initial AlOOH powder; (b) Sample as-sintered by CSP-SPS from the mixture of 95 wt.% AlOOH and 5 wt.%  $\alpha$ -Al<sub>2</sub>O<sub>3</sub> powders.

Most of the bands performed by the sample HA-CS in its IR spectrum (Figure 6a) conformed to the data earlier reported for boehmite [64–67]. Among the observed bands, those at 1065 and 1155 cm<sup>-1</sup> related to symmetric and asymmetric deformation vibrations in hydroxyl groups, while the bands at 3105 and 3296 cm<sup>-1</sup> corresponded to their valence vibrations. The bending mode of the adsorbed water also manifested at 1638 cm<sup>-1</sup>. The bands observed in a range of 487–900 cm<sup>-1</sup> could be assigned to the vibrations in the AlO<sub>6</sub> octahedra, though the position of 721 cm<sup>-1</sup> differed from the literature. In the vicinity to this band, other authors reported the valence vibrations of Al–O in boehmite at 752–770 cm<sup>-1</sup> [64,66]. The observed shift to the lower wavenumber might be caused by the structural transformations of boehmite to  $\gamma$ -alumina, as it was shown above by XRD. Al–O stretching vibrations in  $\alpha$ -alumina located at 447–457 cm<sup>-1</sup> and 488 cm<sup>-1</sup> [68,69] mostly coincided with boehmite bands in the HA-CS spectrum. Thermal treatment of the HA-CS sample led to noticeable changes in IR absorption bands (Figure 6b). AlO<sub>6</sub> valence vibrations in the sample HA-CS-A appeared as a shoulder at 507 cm<sup>-1</sup> as well as a broad band between 630 and 840 cm<sup>-1</sup>. While the least corresponded well to the literature and the data obtained for the commercial  $\alpha$ -alumina powder, as the 507 cm<sup>-1</sup> band was likely to contain unresolved bands located at 487 and 559 cm<sup>-1</sup> (Figure A2). This shifted band location reflected uncompleted structural transformations in HA-CS-A during its annealing. Additionally, the bands at 1037, 1634, 3320, and 3478 cm<sup>-1</sup> assigned to the re-adsorbed water bending preserved in the spectrum of the heated ceramics. The absorption at 2541 cm<sup>-1</sup> could be attributed to the presence of the  $\beta$ -Al<sub>2</sub>O<sub>3</sub> band [70].

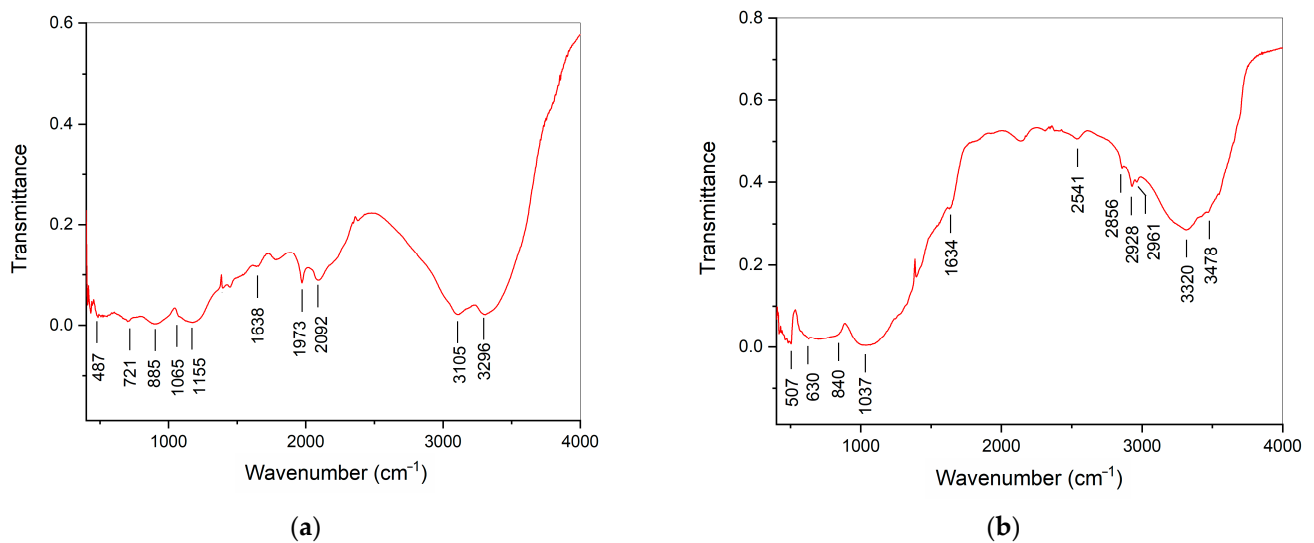


**Figure 6.** Infrared spectra for the ceramic samples prepared from the mixture of  $\gamma$ -Al(OH)<sub>3</sub> and 5 wt.%  $\alpha$ -Al<sub>2</sub>O<sub>3</sub> powders: (a) The sample after CSP-SPS (HA-CS); (b) The sample after CSP-SPS followed by annealing in air at 1250 °C (HA-CS-A).

The sample BO-CS demonstrated high resolution of the absorption bands related to the vibration in the AlO<sub>6</sub> octahedra (487, 554, 630–822 cm<sup>−1</sup>) which pointed to low defect concentration in its structure (Figure 7). Pronounced bands located at 1032, 3292, and 3468 cm<sup>−1</sup> indicated the presence of moisture and hydroxyl groups. The bands at 1977 and 2107 cm<sup>−1</sup> resembled those from the spectrum of boehmite (Figure 6a) and signified that its traces remained in the ceramics after the CSP-SPS.

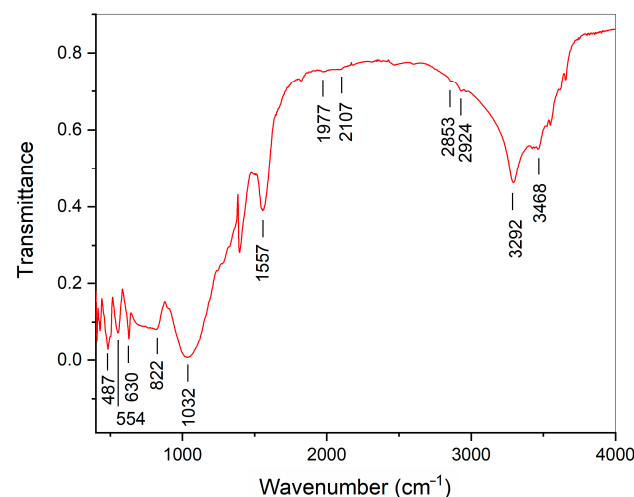


**Figure 7.** Infrared spectrum of the sample BO-CS prepared by CSP-SPS from the mixture of  $\gamma$ -AlOOH and 5 wt.%  $\alpha$ -Al<sub>2</sub>O<sub>3</sub> powders.

Cold sintering of the HA-P powder was accompanied by a preservation of the initial prismatic shape of the hydrargillite crystals in the sample HA-CS (Figure 8a,b). The newly formed prismatic grains in the sample HA-CS demonstrated mostly smooth faces and clear edges. Partial densification occurred due to the destruction of the neighboring particles under the applied pressure, and the porosity after CSP-SPS exceeded 50% (Table 1).



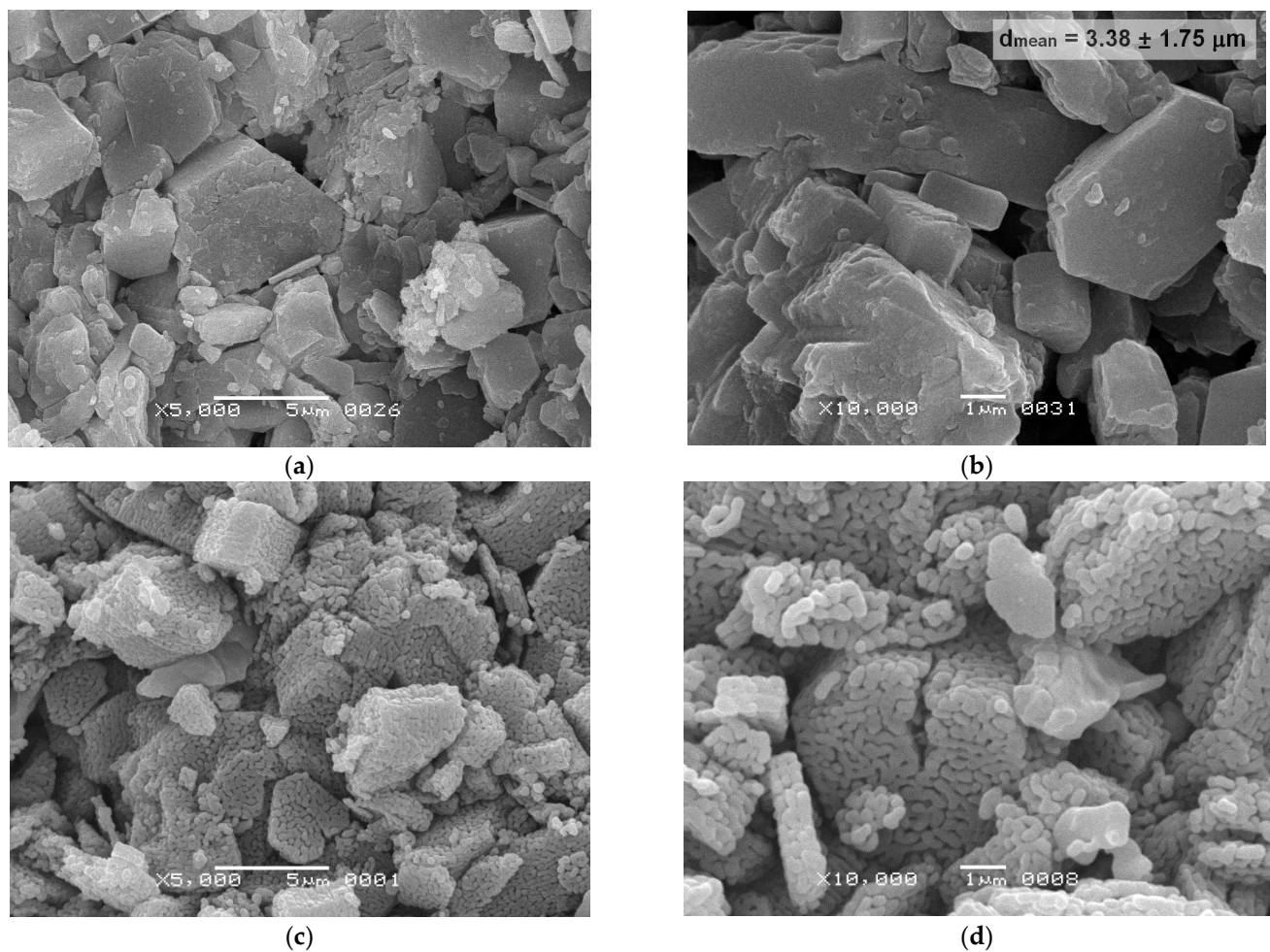


**Figure 8.** SEM images of ceramics fractured surfaces: (a,b) Sample as-sintered by CSP-SPS from the mixture of 95 wt.%  $\gamma$ -Al(OH)<sub>3</sub> and 5 wt.%  $\alpha$ -Al<sub>2</sub>O<sub>3</sub> powders; (c,d) Sample sintered by CSP-SPS from the mixture of 95 wt.%  $\gamma$ -Al(OH)<sub>3</sub> and 5 wt.%  $\alpha$ -Al<sub>2</sub>O<sub>3</sub> powders with further annealing at 1250 °C for 3 h in air.

Annealing of the sample HA-CS in air at 1250 °C for 3 h resulted in the formation of a vermicular structure in HA-CS-A (Figure 8c,d). This type of microstructure was reported to form in alumina ceramics during  $\gamma$ -modification transition into  $\alpha$ -Al<sub>2</sub>O<sub>3</sub> on sintering [71–73]. The appearance of vermicular grains led to the increase of open porosity up to 60% due to the development of the grains' surface (Table 2).

**Table 2.** Integral structural properties of ceramics samples obtained from the mixture of 95 wt.%  $\gamma$ -Al(OH)<sub>3</sub> and 5 wt.%  $\alpha$ -Al<sub>2</sub>O<sub>3</sub>.

Sample	Density after CSP-SPS (g cm <sup>-3</sup> )	Porosity after CSP-SPS (%)	Density after Annealing (g cm <sup>-3</sup> )	Porosity after Annealing (%)
HA-CS 1	1.57	51.9	1.52	60.5
HA-CS 2	1.53	53.3	1.46	60.2
HA-CS 3	1.53	52.9	1.50	60.2

During the CSP-SPS of boehmite powder, a significant grain growth was observed (Figure 9). Compared to the initial  $\gamma$ -AlOOH particles, the mean size of alumina grains increased 4.5 times from 0.65 to 2.94  $\mu$ m. In Figure 9b, one could observe the formation of dense agglomerates of crystals with morphologies similar to that of neighboring non-agglomerated crystals. Due to this partial agglomeration, a large pore space remained

between the crystals of the BO-CS sample. It resulted in a poor transport strength of these ceramics.

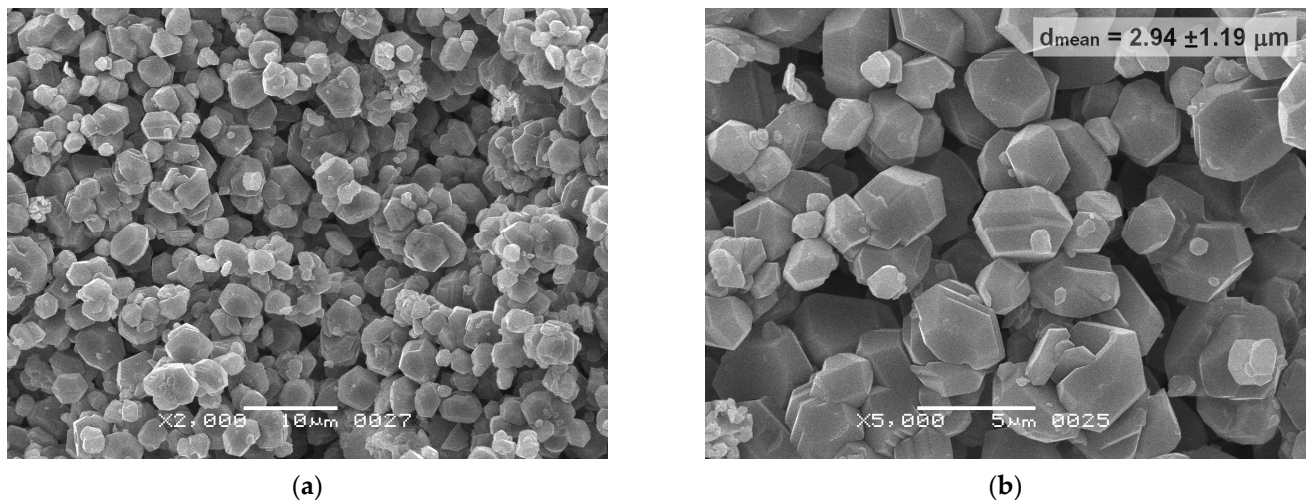


**Figure 9.** SEM images of ceramics fractured surfaces: (a,b) Sample as-sintered by CSP-SPS from the mixture of 95 wt.% AlOOH and 5 wt.%  $\alpha$ -Al<sub>2</sub>O<sub>3</sub> powders (different magnifications).

#### 4. Discussion

For the cold sintering process, the most recognized mechanism is mass transfer due to dissolution—precipitation [21,74], which implies the following stages: (1) powder compaction under mechanical pressure; (2) rearrangement of particles facilitated by the liquid phase; (3) grain growth and closure of pores due to the dissolution of highly stressed points of contacting particles, followed by deposition on non-contacting surfaces with low stress [21]. However, a few subsequent studies have called this model into question showing more complex mechanisms involved in the CSP [75]. Dissolution and precipitation as purely surface phenomena can only lead to coarsening of particles but not contribute to ceramics densification. Additionally, the smallest amount of water sufficient for the CSP could not allow the dissolution of the solid [49]. Considering the role of adsorbed water and its species incorporated in the oxide structure, densification during the CSP was explained by a decrease in the activation energy of atomic diffusion along grain boundaries due to a high concentration of hydroxide ions and other defects [24,25,49].

In this work, during the cold sintering in the SPS machine, hydrargillite and boehmite powders both previously mixed with 5 wt.% of  $\alpha$ -Al<sub>2</sub>O<sub>3</sub> transformed into ceramic materials in the presence of 5 wt.% of distilled water. Boehmite-based powder exposed to CSP-SPS conditions in the presence of water turned into  $\alpha$ -alumina. This result corresponded well to the data on  $\alpha$ -alumina processing in a supercritical water medium [53], where its formation from boehmite occurred directly and bypassed the transient alumina modifications. The traces of remnant boehmite and the presence of trapped water in the prepared ceramics BO-CS pointed to the relation of the CSP-SPS and the processes known for oxides exposed to supercritical water or subcritical vapor [63,76,77]. In that water media, the solid oxides are believed to undergo dissociative adsorption of water molecules which increase the defect concentration in their structure. Gradually, water dissociative adsorption and oxide hydroxylation came to a quasi-equilibrium with water desorption leading to a decreased activation energy of the solid-state transformations [78].

Cold sintering of the hydrargillite-based powder led to the formation of  $\gamma$ -AlOOH as well as  $\gamma$ -Al<sub>2</sub>O<sub>3</sub>, which both inherited the morphology of the initial  $\gamma$ -Al(OH)<sub>3</sub> (Figures 1a and 8a,b). These pseudomorphisms and the presence of  $\gamma$ -Al<sub>2</sub>O<sub>3</sub> pointed to a low pressure of water inside the mold caused by its premature evaporation through gaps between the components of the mold. As a result, the mechanism of phase transitions turned to the usual thermal decomposition of boehmite instead of its direct transformation

to  $\alpha$ -Al<sub>2</sub>O<sub>3</sub> in supercritical water. The pressure of the supercritical water during the preparation of the HA-CS sample appeared too low for the quasi-reversible hydroxylation of boehmite and the promotion of its solid-state mobility. The difference in the decomposition temperatures of  $\gamma$ -AlOOH in the sample HA-CS (526 °C, Figure 4b) compared to the well-crystallized synthesized boehmite (533 °C, Figure 5a) was a consequence of its defective structure.

In the case of the sample BO-CS, heating up to 450 °C resulted in a complete boehmite transformation into  $\alpha$ -Al<sub>2</sub>O<sub>3</sub> due to the preservation of supercritical water inside of the mold. As reported in [54],  $\alpha$ -Al<sub>2</sub>O<sub>3</sub> formation from  $\gamma$ -AlOOH in supercritical water in an autoclave was accompanied by spreading of small boehmite crystals over the surface of larger ones. Due to the mechanical pressure applied during the CSP,  $\alpha$ -Al<sub>2</sub>O<sub>3</sub> crystals in the sample BO-CS agglomerated (Figure 9a). Earlier, a formation of the similar agglomerates was demonstrated in the cold sintering of ZnO ceramics prior to their densification which occurred due to a coalescence of the crystals [77]. The coalescence of ZnO crystals was accompanied by a forced faceting of the newly formed ones and the elimination of the pore space between them. However, in the BO-CS sample, the boundaries were preserved between the crystals in the agglomerates, while the sizes of these crystals remained close to the non-agglomerated crystals (Figure 9a). Hence, the coalescence of the neighboring crystals was hampered by their crystallographic discrepancy. Probably, the crystals in the BO-CS sample possessed a low solid-state mobility for their diffusion re-orientation under the cold sintering conditions. Additionally, the ordering of the  $\alpha$ -Al<sub>2</sub>O<sub>3</sub> structure in the sample BO-CS could occur more rapidly than the re-orientation of the crystallographic planes because of the presence of the initially added  $\alpha$ -alumina [54]. During the rapid ordering of  $\alpha$ -alumina crystals, a major part of the agglomerates was destroyed.

Due to the low pressure of the supercritical water in the mold, the boehmite structure in the HA-CS sample remained poorly ordered and partially transformed in the pseudo-morphic  $\gamma$ -Al<sub>2</sub>O<sub>3</sub> during the CSP. Further lowering of the pressure supposedly would lead to the formation of tohdite 5Al<sub>2</sub>O<sub>3</sub>·H<sub>2</sub>O instead of boehmite; similarly, it was shown for hydrogillite treatment in an autoclave at different ratios of supercritical water to alumina [79]. Tohdite is known to transform into  $\kappa$ -Al<sub>2</sub>O<sub>3</sub> at a temperature above 700 °C [80,81].

High-temperature annealing of the cold-sintered ceramics HA-CS resulted in the formation of  $\alpha$ -alumina ceramics with considerable porosity of about 60% (HA-CS-A). The obtained value was comparable to those reported earlier for technical porous alumina ceramics. In recent works, the obtaining of alumina ceramics with porosity of about 54% was reported in a context of indirect selective laser sintering applications [82]. The foaming process with the use of natural agents allowed higher porosities of 80–87% to be reached [83]. The ceramics prepared in the current work by CSP-SPS were promising for further investigation of their structural and mechanical properties and their tailoring by variation of the sintering conditions.

For the moment, the reproducible preparation of the  $\alpha$ -Al<sub>2</sub>O<sub>3</sub> material with the use of CSP-SPS in the presence of water as a transient liquid was limited by the constriction of the mold. A disadvantage of the currently used mold was connected to an insufficient reproducibility of its sealing. Previously, the importance of the mold sealing system and the choice of appropriate materials for it was demonstrated in the cold sintering of ZnO ceramics [84]. The improvement of the mold design would allow for the preservation of the CSP-SPS conditions for a longer exposure and open prospects in obtaining dense  $\alpha$ -alumina ceramics by a novel ecologically pure and energy-saving technique.



## 5. Conclusions

The current work detailed a new processing route for  $\alpha$ - $\text{Al}_2\text{O}_3$  ceramics which involved cold sintering using SPS equipment in the presence of only distilled water as a transient liquid. The study of phase contents, thermal behavior, and microstructure of the cold-sintered ceramics pointed to the vicinity of mechanisms governing this sintering process and the transformations in oxides in vapor and supercritical water. In this case, the decisive role in the sintering belonged to the processes of intense hydroxylation and dehydroxylation of the solid rather than its dissolution. Due to the second annealing in air, the cold-sintered material mostly consisting of boehmite was successfully transformed into  $\alpha$ - $\text{Al}_2\text{O}_3$  ceramics with a vermicular structure and porosity of about 60%. Further improvements of the cold sintering design and adjustment of its regimens would open prospects for an economical and ecologically benign route to  $\alpha$ -alumina ceramics.

**Author Contributions:** Conceptualization, A.A.K., A.V.S. and Y.D.I.; methodology, A.A.K., A.V.S. and Y.D.I.; validation, A.V.S. and Y.D.I.; investigation, M.V.K., M.A.P., A.V.S. and Y.D.I.; resources, A.A.K., A.V.S. and Y.D.I.; data curation, A.A.K., M.V.K., A.V.S. and Y.D.I.; writing—original draft preparation, A.A.K., A.V.S. and Y.D.I.; writing—review and editing, A.A.K. and A.V.S.; visualization, A.A.K.; supervision, A.A.K., A.V.S. and Y.D.I.; project administration, A.A.K.; funding acquisition, A.A.K. All authors have read and agreed to the published version of the manuscript.

**Funding:** This research was funded by the Russian Science Foundation, grant number 22-73-00318.

**Institutional Review Board Statement:** Not applicable.

**Informed Consent Statement:** Not applicable.

**Data Availability Statement:** The data presented in this study are available upon request from the corresponding author after obtaining the permission of an authorized person.

**Acknowledgments:** The authors are thankful to their colleagues from Lomonosov MSU, Chemistry Department: to S.Yu. Kupreenko and A.V. Shumyantsev for their help in thermal analysis; to A.N. Kharlanov for his help with IR spectroscopy. The work was supported in part by the Lomonosov Moscow State University Program of Development.

**Conflicts of Interest:** The authors declare no conflict of interest.

## Appendix A

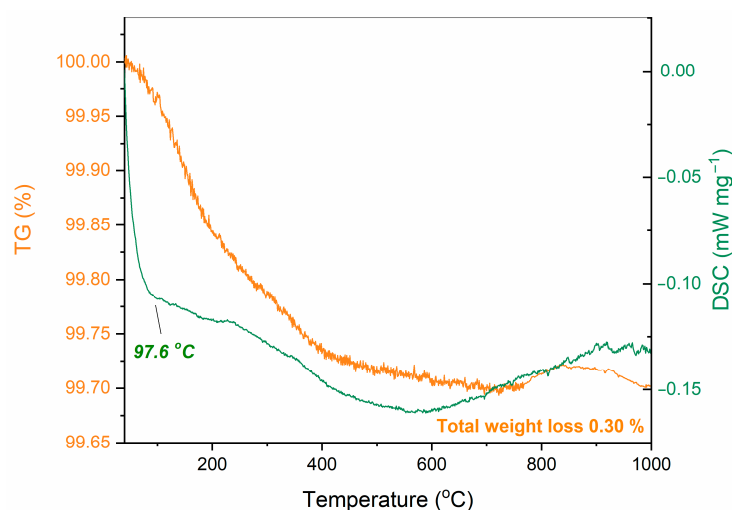


**Figure A1.** Thermal analysis of a commercial  $\alpha$ - $\text{Al}_2\text{O}_3$  powder.



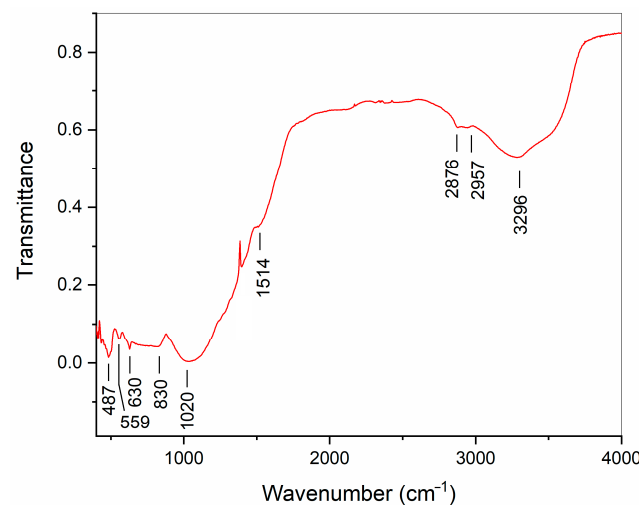


**Figure A2.** Infrared spectrum of a commercial  $\alpha$ -Al<sub>2</sub>O<sub>3</sub> powder.

## References

- Ohji, T.; Fukushima, M. Macro-Porous Ceramics: Processing and Properties. *Int. Mater. Rev.* **2012**, *57*, 115–131. [\[CrossRef\]](#)
- Hardy, D.; Green, D.J. Mechanical Properties of a Partially Sintered Alumina. *J. Eur. Ceram. Soc.* **1995**, *15*, 769–775. [\[CrossRef\]](#)
- Çelik, A.; Çağlar, G.; Çelik, Y. Fabrication of Porous Al<sub>2</sub>O<sub>3</sub> Ceramics Using Carbon Black as a Pore Forming Agent by Spark Plasma Sintering. *Ceram. Int.* **2022**, *48*, 28181–28190. [\[CrossRef\]](#)
- González-Sánchez, M.; Rivero-Antúnez, P.; Cano-Crespo, R.; Morales-Flórez, V. Fabrication of Porous Alumina Structures by SPS and Carbon Sacrificial Template for Bone Regeneration. *Materials* **2022**, *15*, 1754. [\[CrossRef\]](#) [\[PubMed\]](#)
- Chen, C.; Ding, X.; Wang, Y.; Luo, Z.; Zhai, P. Fractal Dimension Analysis of Structure and Bending Strength of Porous Alumina Prepared Using Starch and Carbon Fiber as Pore-Forming Agents. *Fractal Fract.* **2022**, *6*, 574. [\[CrossRef\]](#)
- Biggemann, J.; Stumpf, M.; Fey, T. Porous Alumina Ceramics with Multimodal Pore Size Distributions. *Materials* **2021**, *14*, 3294. [\[CrossRef\]](#) [\[PubMed\]](#)
- Schelm, K.; Fey, T.; Dammler, K.; Betke, U.; Scheffler, M. Hierarchical-Porous Ceramic Foams by a Combination of Replica and Freeze Technique. *Adv. Eng. Mater.* **2019**, *21*, 1801362. [\[CrossRef\]](#)
- Scheithauer, U.; Kerber, F.; Füssel, A.; Holtzhausen, S.; Beckert, W.; Schwarzer, E.; Weingarten, S.; Michaelis, A. Alternative Process Routes to Manufacture Porous Ceramics—Opportunities and Challenges. *Materials* **2019**, *12*, 663. [\[CrossRef\]](#)
- He, X.; Zhou, X.; Su, B. 3D Interconnective Porous Alumina Ceramics via Direct Protein Foaming. *Mater. Lett.* **2009**, *63*, 830–832. [\[CrossRef\]](#)
- Devavarapu, S.; Chaudhuri, P.; Shrivastava, A.; Bhattacharyya, S. Processing of Porous Alumina by Foaming Method-Effect of Foaming Agent, Solid Loading and Binder. *Ceram. Int.* **2019**, *45*, 12264–12273. [\[CrossRef\]](#)
- Maria, J.-P.; Kang, X.; Floyd, R.D.; Dickey, E.C.; Guo, H.; Guo, J.; Baker, A.; Funihashi, S.; Randall, C.A. Cold Sintering: Current Status and Prospects. *J. Mater. Res.* **2017**, *32*, 3205–3218. [\[CrossRef\]](#)
- Langer, J.; Hoffmann, M.J.; Guillon, O. Direct Comparison between Hot Pressing and Electric Field-Assisted Sintering of Submicron Alumina. *Acta Mater.* **2009**, *57*, 5454–5465. [\[CrossRef\]](#)
- Bocanegra-Bernal, M.H. Hot Isostatic Pressing (HIP) Technology and Its Applications to Metals and Ceramics. *J. Mater. Sci.* **2004**, *39*, 6399–6420. [\[CrossRef\]](#)
- Oghbaei, M.; Mirzaee, O. Microwave versus Conventional Sintering: A Review of Fundamentals, Advantages and Applications. *J. Alloys Compd.* **2010**, *494*, 175–189. [\[CrossRef\]](#)
- Munir, Z.A.; Quach, D.V.; Ohyanagi, M. Electric Current Activation of Sintering: A Review of the Pulsed Electric Current Sintering Process: Electric Current Activation of Sintering. *J. Am. Ceram. Soc.* **2011**, *94*, 1–19. [\[CrossRef\]](#)
- Munir, Z.A.; Anselmi-Tamburini, U.; Ohyanagi, M. The Effect of Electric Field and Pressure on the Synthesis and Consolidation of Materials: A Review of the Spark Plasma Sintering Method. *J. Mater. Sci.* **2006**, *41*, 763–777. [\[CrossRef\]](#)
- Rubinovskii, N.A.; Shornikov, D.P.; Tenishev, A.V.; Zaluzhnyi, A.G.; Zholnin, A.G. Effect of Aluminum Oxide Powder Particle Size on Spark Plasma Sintering Results. *Glass Ceram.* **2019**, *76*, 94–98. [\[CrossRef\]](#)
- Wang, S.W.; Chen, L.D.; Hirai, T. Densification of Al<sub>2</sub>O<sub>3</sub> Powder Using Spark Plasma Sintering. *J. Mater. Res.* **2000**, *15*, 982–987. [\[CrossRef\]](#)
- Young, C.; Zhang, C.; Nisar, A.; Boesl, B.; Agarwal, A. Spark Plasma Sintered Porous Aluminum Oxide for Filtration Applications. *Ceram. Int.* **2021**, *47*, 21822–21827. [\[CrossRef\]](#)
- Roussel, N.; Lallemand, L.; Chane-Ching, J.-Y.; Guillemet-Fristch, S.; Durand, B.; Garnier, V.; Bonnefont, G.; Fantozzi, G.; Bonneau, L.; Trombert, S.; et al. Highly Dense, Transparent  $\alpha$ -Al<sub>2</sub>O<sub>3</sub> Ceramics From Ultrafine Nanoparticles Via a Standard SPS Sintering. *J. Am. Ceram. Soc.* **2013**, *96*, 1039–1042. [\[CrossRef\]](#)

21. Guo, J.; Guo, H.; Baker, A.L.; Lanagan, M.T.; Kupp, E.R.; Messing, G.L.; Randall, C.A. Cold Sintering: A Paradigm Shift for Processing and Integration of Ceramics. *Angew. Chem. Int. Ed.* **2016**, *55*, 11457–11461. [[CrossRef](#)] [[PubMed](#)]
22. Ibn-Mohammed, T.; Randall, C.A.; Mustapha, K.B.; Guo, J.; Walker, J.; Berbano, S.; Koh, S.C.L.; Wang, D.; Sinclair, D.C.; Reaney, I.M. Decarbonising Ceramic Manufacturing: A Techno-Economic Analysis of Energy Efficient Sintering Technologies in the Functional Materials Sector. *J. Eur. Ceram. Soc.* **2019**, *39*, 5213–5235. [[CrossRef](#)]
23. Floyd, R.D.; Lowum, S.; Maria, J.-P. Cold Sintering Zinc Oxide with a Crystalline Zinc Acetate Dihydrate Mass Transport Phase. *J. Mater. Sci.* **2020**, *55*, 15117–15129. [[CrossRef](#)]
24. Dargatz, B.; Gonzalez-Julian, J.; Bram, M.; Jakes, P.; Besmehn, A.; Schade, L.; Röder, R.; Ronning, C.; Guillon, O. FAST/SPS Sintering of Nanocrystalline Zinc Oxide—Part I: Enhanced Densification and Formation of Hydrogen-Related Defects in Presence of Adsorbed Water. *J. Eur. Ceram. Soc.* **2016**, *36*, 1207–1220. [[CrossRef](#)]
25. Dargatz, B.; Gonzalez-Julian, J.; Bram, M.; Shinoda, Y.; Wakai, F.; Guillon, O. FAST/SPS Sintering of Nanocrystalline Zinc Oxide—Part II: Abnormal Grain Growth, Texture and Grain Anisotropy. *J. Eur. Ceram. Soc.* **2016**, *36*, 1221–1232. [[CrossRef](#)]
26. Ivakin, Y.; Smirnov, A.; Kholodkova, A.; Vasin, A.; Kormilicyn, M.; Korniyushin, M.; Stolyarov, V. Comparative Study of Cold Sintering Process and Autoclave Thermo-Vapor Treatment on a ZnO Sample. *Crystals* **2021**, *11*, 71. [[CrossRef](#)]
27. Bang, S.H.; Tsuji, K.; Ndayishimiye, A.; Dursun, S.; Seo, J.; Otieno, S.; Randall, C.A. Toward a Size Scale-up Cold Sintering Process at Reduced Uniaxial Pressure. *J. Am. Ceram. Soc.* **2020**, *103*, 2322–2327. [[CrossRef](#)]
28. Hérisson de Beauvoir, T.; Dursun, S.; Gao, L.; Randall, C. New Opportunities in Metallization Integration in Cofired Electroceramic Multilayers by the Cold Sintering Process. *ACS Appl. Electron. Mater.* **2019**, *1*, 1198–1207. [[CrossRef](#)]
29. Jing, Y.; Luo, N.; Wu, S.; Han, K.; Wang, X.; Miao, L.; Wei, Y. Remarkably Improved Electrical Conductivity of ZnO Ceramics by Cold Sintering and Post-Heat-Treatment. *Ceram. Int.* **2018**, *44*, 20570–20574. [[CrossRef](#)]
30. Funahashi, S.; Guo, J.; Guo, H.; Wang, K.; Baker, A.L.; Shiratsuyu, K.; Randall, C.A. Demonstration of the Cold Sintering Process Study for the Densification and Grain Growth of ZnO Ceramics. *J. Am. Ceram. Soc.* **2017**, *100*, 546–553. [[CrossRef](#)]
31. Ma, J.-P.; Chen, X.-M.; Ouyang, W.-Q.; Wang, J.; Li, H.; Fang, J.-L. Microstructure, Dielectric, and Energy Storage Properties of BaTiO<sub>3</sub> Ceramics Prepared via Cold Sintering. *Ceram. Int.* **2018**, *44*, 4436–4441. [[CrossRef](#)]
32. Tsuji, K.; Ndayishimiye, A.; Lowum, S.; Floyd, R.; Wang, K.; Wetherington, M.; Maria, J.-P.; Randall, C.A. Single Step Densification of High Permittivity BaTiO<sub>3</sub> Ceramics at 300 °C. *J. Eur. Ceram. Soc.* **2020**, *40*, 1280–1284. [[CrossRef](#)]
33. Sada, T.; Ndayishimiye, A.; Fan, Z.; Fujioka, Y.; Randall, C.A. Surface Modification of BaTiO<sub>3</sub> with Catechol Surfactant and Effects on Cold Sintering. *J. Appl. Phys.* **2021**, *129*, 184102. [[CrossRef](#)]
34. Guo, N.; Shen, H.-Z.; Shen, P. One-Step Synthesis and Densification of BaTiO<sub>3</sub> by Reactive Cold Sintering. *Scr. Mater.* **2022**, *213*, 114628. [[CrossRef](#)]
35. Ma, J.; Li, H.; Wang, H.; Lin, C.; Wu, X.; Lin, T.; Zheng, X.; Yu, X. Composition, Microstructure and Electrical Properties of K<sub>0.5</sub>Na<sub>0.5</sub>NbO<sub>3</sub> Ceramics Fabricated by Cold Sintering Assisted Sintering. *J. Eur. Ceram. Soc.* **2019**, *39*, 986–993. [[CrossRef](#)]
36. Chi, M.; Ma, W.; Guo, J.; Wu, J.; Li, T.; Wang, S.; Zhang, P. Effect of NaCl on the Microstructure and Electrical Properties of K<sub>0.5</sub>Na<sub>0.5</sub>NbO<sub>3</sub> Ceramics Prepared by Cold Sintering Process. *J. Mater. Sci. Mater. Electron.* **2019**, *30*, 21435–21443. [[CrossRef](#)]
37. Cong, L.; Huajing, W.; Jianzhang, M.; Baoyu, D.; Xiao, W.; Tengfei, L.; Xinghua, Z.; Xing, Y. Effect of Dwell Time on Cold Sintering Assisted Sintering Based Highly Transparent 0.9K<sub>0.5</sub>Na<sub>0.5</sub>NbO<sub>3</sub>-0.1LiBiO<sub>3</sub> Ceramics. *J. Alloys Compd.* **2020**, *826*, 154249. [[CrossRef](#)]
38. Tsuji, K.; Fan, Z.; Bang, S.H.; Dursun, S.; Trolrier-McKinstry, S.; Randall, C.A. Cold Sintering of the Ceramic Potassium Sodium Niobate, (K<sub>0.5</sub>Na<sub>0.5</sub>)NbO<sub>3</sub>, and Influences on Piezoelectric Properties. *J. Eur. Ceram. Soc.* **2022**, *42*, 105–111. [[CrossRef](#)]
39. Wang, D.; Guo, H.; Morandi, C.S.; Randall, C.A.; Trolrier-McKinstry, S. Cold Sintering and Electrical Characterization of Lead Zirconate Titanate Piezoelectric Ceramics. *APL Mater.* **2018**, *6*, 016101. [[CrossRef](#)]
40. Wang, D.; Tsuji, K.; Randall, C.A.; Trolrier-McKinstry, S. Model for the Cold Sintering of Lead Zirconate Titanate Ceramic Composites. *J. Am. Ceram. Soc.* **2020**, *103*, 4894–4902. [[CrossRef](#)]
41. Wang, D.; Dursun, S.; Gao, L.; Morandi, C.S.; Randall, C.A.; Trolrier-McKinstry, S. Fabrication of Bimorph Lead Zirconate Titanate Thick Films on Metal Substrates via the Cold Sintering-Assisted Process. *Acta Mater.* **2020**, *195*, 482–490. [[CrossRef](#)]
42. Induja, I.J.; Sebastian, M.T. Microwave Dielectric Properties of Cold Sintered Al<sub>2</sub>O<sub>3</sub>-NaCl Composite. *Mater. Lett.* **2018**, *211*, 55–57. [[CrossRef](#)]
43. Suleiman, B.; Zhang, H.; Ding, Y.; Li, Y. Microstructure and Mechanical Properties of Cold Sintered Porous Alumina Ceramics. *Ceram. Int.* **2022**, *48*, 13531–13540. [[CrossRef](#)]
44. Akmal, M.; Hassan, M.; Afzal, M.; Ryu, H.J. Novel Approach to Sintering Hydroxyapatite-Alumina Nanocomposites at 300 °C. *Mater. Chem. Phys.* **2021**, *260*, 124187. [[CrossRef](#)]
45. Hérisson de Beauvoir, T.; Estournès, C. Translucent  $\gamma$ -AlOOH and  $\gamma$ -Al<sub>2</sub>O<sub>3</sub> Glass-Ceramics Using the Cold Sintering Process. *Scr. Mater.* **2021**, *194*, 113650. [[CrossRef](#)]
46. Kang, S.; Zhao, X.; Guo, J.; Liang, J.; Sun, J.; Yang, Y.; Yang, L.; Liao, R.; Randall, C.A. Thermal-Assisted Cold Sintering Study of Al<sub>2</sub>O<sub>3</sub> Ceramics: Enabled with a Soluble  $\gamma$ -Al<sub>2</sub>O<sub>3</sub> Intermediate Phase. *J. Eur. Ceram. Soc.* **2023**, *43*, 478–485. [[CrossRef](#)]
47. Herisson de Beauvoir, T.; Sangregorio, A.; Cornu, I.; Elissalde, C.; Josse, M. Cool-SPS: An Opportunity for Low Temperature Sintering of Thermodynamically Fragile Materials. *J. Mater. Chem. C* **2018**, *6*, 2229–2233. [[CrossRef](#)]
48. Schwarz, S.; Thron, A.M.; Rufner, J.; Benthem, K.; Guillon, O. Low Temperature Sintering of Nanocrystalline Zinc Oxide: Effect of Heating Rate Achieved by Field Assisted Sintering/Spark Plasma Sintering. *J. Am. Ceram. Soc.* **2012**, *95*, 2451–2457. [[CrossRef](#)]

49. Gonzalez-Julian, J.; Neuhaus, K.; Bernemann, M.; Pereira da Silva, J.; Laptev, A.; Bram, M.; Guillon, O. Unveiling the Mechanisms of Cold Sintering of ZnO at 250 °C by Varying Applied Stress and Characterizing Grain Boundaries by Kelvin Probe Force Microscopy. *Acta Mater.* **2018**, *144*, 116–128. [\[CrossRef\]](#)
50. Nur, K.; Mishra, T.P.; da Silva, J.G.P.; Gonzalez-Julian, J.; Bram, M.; Guillon, O. Influence of Powder Characteristics on Cold Sintering of Nano-Sized ZnO with Density above 99%. *J. Eur. Ceram. Soc.* **2021**, *41*, 2648–2662. [\[CrossRef\]](#)
51. Liang, J.; Zhao, X.; Kang, S.; Guo, J.; Chen, Z.; Long, Y.; Zeng, Q.; Sun, J.; Yang, L.; Liao, R.; et al. Microstructural Evolution of ZnO via Hybrid Cold Sintering/Spark Plasma Sintering. *J. Eur. Ceram. Soc.* **2022**, *42*, 5738–5746. [\[CrossRef\]](#)
52. Ivakin, Y.D.; Smirnov, A.V.; Kurmysheva, A.Y.; Kharlanov, A.N.; Solís Pinargote, N.W.; Smirnov, A.; Grigoriev, S.N. The Role of the Activator Additives Introduction Method in the Cold Sintering Process of ZnO Ceramics: CSP/SPS Approach. *Materials* **2021**, *14*, 6680. [\[CrossRef\]](#)
53. Lazarev, V.B.; Panasyuk, G.P.; Voroshilov, I.L.; Boudova, G.P.; Danchevskaya, M.N.; Torbin, S.N.; Ivakin, Y.D. New Ecologically Pure Technologies of Fine-Crystalline Materials. *Ind. Eng. Chem. Res.* **1996**, *35*, 3721–3725. [\[CrossRef\]](#)
54. Ivakin, Y.D.; Danchevskaya, M.N.; Muravieva, G.P. Induced Formation of Corundum Crystals in Supercritical Water Fluid. *Russ. J. Phys. Chem. B* **2015**, *9*, 1082–1094. [\[CrossRef\]](#)
55. Gates-Rector, S.; Blanton, T. The Powder Diffraction File: A Quality Materials Characterization Database. *Powder Diffr.* **2019**, *34*, 352–360. [\[CrossRef\]](#)
56. Schneider, C.A.; Rasband, W.S.; Eliceiri, K.W. NIH Image to ImageJ: 25 Years of Image Analysis. *Nat. Methods* **2012**, *9*, 671–675. [\[CrossRef\]](#)
57. Stevens, R. Beta-Alumina. In *Concise Encyclopedia of Advanced Ceramic Materials*; Elsevier: Amsterdam, The Netherlands, 1991; pp. 32–35. ISBN 978-0-08-034720-2.
58. Danchevskaya, M.N.; Ivakin, Y.D.; Torbin, S.N.; Panasyuk, G.P.; Belan, V.N.; Voroshilov, I.L. Scientific Basis of Technology of Fine-Crystalline Quartz and Corundum. *High Press. Res.* **2001**, *20*, 229–239. [\[CrossRef\]](#)
59. Sato, T. Thermal Decomposition of Aluminium Hydroxides. *J. Therm. Anal.* **1987**, *32*, 61–70. [\[CrossRef\]](#)
60. Lamouri, S.; Hamidouche, M.; Bouaouadja, N.; Belhouchet, H.; Garnier, V.; Fantozzi, G.; Trekat, J.F. Control of the  $\gamma$ -Alumina to  $\alpha$ -Alumina Phase Transformation for an Optimized Alumina Densification. *Bol. Soc. Esp. Ceram. Vidr.* **2017**, *56*, 47–54. [\[CrossRef\]](#)
61. Panasyuk, G.P.; Kozerozhets, I.V.; Semenov, E.A.; Danchevskaya, M.N.; Azarova, L.A.; Belan, V.N. Thermodynamics and Kinetics of  $\gamma$ -Al<sub>2</sub>O<sub>3</sub> and AlOOH Transformations under Hydrothermal Conditions. *Inorg. Mater.* **2019**, *55*, 920–928. [\[CrossRef\]](#)
62. Kozerozhets, I.V.; Panasyuk, G.P.; Semenov, E.A.; Danchevskaya, M.N.; Azarova, L.A.; Simonenko, N.P. Transformations of Nanosized Boehmite and  $\gamma$ -Al<sub>2</sub>O<sub>3</sub> upon Heat Treatment. *Russ. J. Inorg. Chem.* **2020**, *65*, 587–591. [\[CrossRef\]](#)
63. Maryashkin, A.V.; Ivakin, Y.D.; Danchevskaya, M.N.; Murav'eva, G.P.; Kirikova, M.N. Synthesis of Corundum Doped with Cerium in Supercritical Water Fluid. *Moscow Univ. Chem. Bull.* **2011**, *66*, 290–298. [\[CrossRef\]](#)
64. Kiss, A.B.; Keresztury, G.; Farkas, L. Raman and i.r. Spectra and Structure of Boehmite ( $\gamma$ -AlOOH). Evidence for the Recently Discarded D<sup>17</sup><sub>2h</sub> Space Group. *Spectrochim. Acta Part A* **1980**, *36A*, 653–658. [\[CrossRef\]](#)
65. Abdollahifar, M.; Zamani, R.; Beigy, E.; Nekouei, H. Synthesis of Micro-Mesopores Flowerlike  $\gamma$ -Al<sub>2</sub>O<sub>3</sub> Nano-Architectures. *J. Serb. Chem. Soc.* **2014**, *79*, 1007–1017. [\[CrossRef\]](#)
66. Sun, T.; Zhuo, Q.; Chen, Y.; Wu, Z. Synthesis of Boehmite and Its Effect on Flame Retardancy of Epoxy Resin. *High Perform. Polym.* **2015**, *27*, 100–104. [\[CrossRef\]](#)
67. Klopogge, J.T.; Ruan, H.D.; Frost, R.L. Thermal Decomposition of Bauxite Minerals: Infrared Emission Spectroscopy of Gibbsite, Boehmite and Diaspore. *J. Mater. Sci.* **2002**, *37*, 1121–1129. [\[CrossRef\]](#)
68. Hajduchova, Z. Adsorption of Dodecylbenzenesulfonic Acid on the Alumina Particles in the Preparation of Alumina Foam. *Ceram.-Silik.* **2018**, *62*, 138–145. [\[CrossRef\]](#)
69. Santhiya, D.; Subramanian, S.; Natarajan, K.A.; Malghan, S.G. Surface Chemical Studies on Alumina Suspensions Using Ammonium Poly(Methacrylate). *Colloids Surf.* **2000**, *164*, 143–154. [\[CrossRef\]](#)
70. Colombari, P. Vibrational Characterization of the Various Forms of (Solvated or Unsolvated) Mobile Proton in the Solid State. Advantages, Limitations and Open Questions. *Solid State Ion.* **2023**, *393*, 116187. [\[CrossRef\]](#)
71. Wang, L.; Hu, J.; Cheng, Y.; Fu, Z.; Shen, Z.; Xiong, Y. Defect Formation by Order Coalescence in Vermicular Grains during Alumina Phase Transformation. *Scr. Mater.* **2015**, *107*, 59–62. [\[CrossRef\]](#)
72. Jiménez-Morales, F.; Rivero-Antúnez, P.; González-Sánchez, M.; Garrido-Regife, L.; Morales-Flórez, V. The Evolution of Vermicular Structures and Sintering Behavior of Alumina. In *Cellular Automata*; Chopard, B., Bandini, S., Dennunzio, A., Arabi Haddad, M., Eds.; Lecture Notes in Computer Science; Springer International Publishing: Cham, Switzerland, 2022; Volume 13402, pp. 153–162. ISBN 978-3-031-14925-2.
73. Dutta, S.; Kim, T.B.; Krentz, T.; Vinci, R.P.; Chan, H.M. Sol-Gel-Derived Single-Crystal Alumina Coatings with Vermicular Structure: Rapid Communications of the American Ceramic Society. *J. Am. Ceram. Soc.* **2011**, *94*, 340–343. [\[CrossRef\]](#)
74. Guo, J.; Floyd, R.; Lowum, S.; Maria, J.-P.; Herisson de Beauvoir, T.; Seo, J.-H.; Randall, C.A. Cold Sintering: Progress, Challenges, and Future Opportunities. *Annu. Rev. Mater. Res.* **2019**, *49*, 275–295. [\[CrossRef\]](#)
75. Grasso, S.; Biesuz, M.; Zoli, L.; Taveri, G.; Duff, A.I.; Ke, D.; Jiang, A.; Reece, M.J. A Review of Cold Sintering Processes. *Adv. Appl. Ceram.* **2020**, *119*, 115–143. [\[CrossRef\]](#)
76. Kholodkova, A.A.; Danchevskaya, M.N.; Ivakin, Y.D.; Muravieva, G.P.; Tyablikov, A.S. Crystalline Barium Titanate Synthesized in Sub- and Supercritical Water. *J. Supercrit. Fluids* **2016**, *117*, 194–202. [\[CrossRef\]](#)

77. Ivakin, Y.D.; Danchevskaya, M.N.; Muravieva, G.P. Recrystallization of Zinc Oxide in a Sub- and Supercritical Water Medium. *Russ. J. Phys. Chem. B* **2019**, *13*, 1189–1200. [[CrossRef](#)]
78. Kozawa, T.; Onda, A.; Yanagisawa, K. Accelerated Formation of Barium Titanate by Solid-State Reaction in Water Vapour Atmosphere. *J. Eur. Ceram. Soc.* **2009**, *29*, 3259–3264. [[CrossRef](#)]
79. Ivakin, Y.D.; Danchevskaya, M.N.; Muravieva, G.P. Influence of Molar Ratio Water Fluid/ $\text{Al}_2\text{O}_3$  on Solid Phase Composition. In Proceedings of the 9th Meeting of Supercritical Fluids, Trieste, Italy, 13–16 June 2004. 24. [[CrossRef](#)]
80. Okumiya, M.; Yamaguchi, G.; Yamada, O.; Ono, S. Formation of  $\kappa$ - and  $\kappa'$ -aluminium oxide from the dehydration of tohdite ( $5\text{Al}_2\text{O}_3 \cdot \text{H}_2\text{O}$ ). *Bull. Chem. Soc. Jpn.* **1971**, *44*, 418–423. [[CrossRef](#)]
81. De Bellis, J.; Ochoa-Hernández, C.; Farès, C.; Petersen, H.; Ternienden, J.; Weidenthaler, C.; Amrute, A.P.; Schüth, F. Surface and Bulk Chemistry of Mechanochemically Synthesized Tohdite Nanoparticles. *J. Am. Chem. Soc.* **2022**, *144*, 9421–9433. [[CrossRef](#)]
82. Dong, Y.; Jiang, H.; Chen, A.; Yang, T.; Zou, T.; Xu, D. Porous  $\text{Al}_2\text{O}_3$  Ceramics with Spontaneously Formed Pores and Enhanced Strength Prepared by Indirect Selective Laser Sintering Combined with Reaction Bonding. *Ceram. Int.* **2020**, *46*, 15159–15166. [[CrossRef](#)]
83. Xu, C.; Liu, H.; Yang, H.; Yang, L. A Green Biocompatible Fabrication of Highly Porous Functional Ceramics with High Strength and Controllable Pore Structures. *J. Mater. Sci. Technol.* **2016**, *32*, 729–732. [[CrossRef](#)]
84. Smirnov, A.V.; Korniyushin, M.V.; Kholodkova, A.A.; Melnikov, S.A.; Stepanov, A.D.; Fesik, E.V.; Ivakin, Y.D. Cold Sintering Process of Zinc Oxide Ceramics: Powder Preparation and Sintering Conditions Effects on Final Microstructure. *Inorganics* **2022**, *10*, 197. [[CrossRef](#)]

**Disclaimer/Publisher's Note:** The statements, opinions and data contained in all publications are solely those of the individual author(s) and contributor(s) and not of MDPI and/or the editor(s). MDPI and/or the editor(s) disclaim responsibility for any injury to people or property resulting from any ideas, methods, instructions or products referred to in the content.